Research Square

Preprints are preliminary reports that have not undergone peer review.
They should not be considered conclusive, used to inform clinical practice,
or referenced by the media as validated information.

Volume scattering of radar signals is not a single diagnostic indicator of water ice within permanently shadowed regions near the lunar poles

sriram saran

sriram.saran@gmail.com

Indian Space Research Organisation https://orcid.org/0000-0003-0019-6261

Tathagata Chakraborty

Indian Space Research Organisation

Bradley Thomson

University of Tennessee at Knoxville

Edgard G. Rivera-Valentin

Johns Hopkins University Applied Physics Laboratory

Raghav Mehra

Indian Space Research Organisation

Deepak Putrevu

Indian Space Research Organisation

Research Article

Keywords: Radar, polarimetry, craters, lunar poles, ice

Posted Date: July 23rd, 2026

DOI: https://doi.org/10.21203/rs.3.rs-10440691/v1

License: This work is licensed under a Creative Commons Attribution 4.0 International License.
Read Full License

Additional Declarations: The authors declare no competing interests.

Abstract

Recently, Sinha et al. interpreted polarimetric radar signatures from the interiors of some doubly shadowed craters near the lunar South Pole as evidence for subsurface ice. They proposed a combined empirical threshold for radar circular polarization ratio (CPR) and the degree of polarization (DOP) as a refined diagnostic criterion for identifying subsurface ice through volume scattering. We argue instead that these variations in CPR and DOP are fully consistent with different levels of near-surface roughness within these craters, and the proposed threshold values are not a definitive indicator of volume scattering caused by subsurface ice. When observed using fully polarimetric radar data, robust evidence for thick, sheet-like water ice within the lunar poles require a combination of strong linear, circular polarization ratios, and enhanced DOP values, along with a high degree of correlation between radar-bright features and regions of permanent shadow.

Erroneous expression for the radar circular polarization ratio

The formula used in Sinha et al.[1] to generate the radar circular polarization ratio (CPR) from DFSAR data is incorrect. CPR is defined as the ratio of the backscattered power coefficients in the same-sense circular (σ°_{SC}) to the opposite-sense circular (σ°_{OC}) polarization as transmitted (i.e., CPR= $\sigma^\circ_{SC}/\sigma^\circ_{OC}$). The CPR equation used in Sinha et al[1], though, only applies to the special case of dihedral scatterers where there are no cross-pol (HV/VH) components, and is uncommon for natural surfaces (**ref. 2**). We have generated the CPR images using equations 1, 2 as given in the Methods (supplementary information) and sampled the interiors (Supplementary figure S1) of the 10 south polar craters as given in Tables 1, 2 in **ref. 1**. For three craters F2 (Faustini), S1, H1, we made a scatter plot of CPR values generated from both the formulas, as shown in Figure 1. Along with this, we generated the statistical distributions in the form of a box and whisker plot for each of the 10 craters as shown in supplementary figure S2. Large differences in the distribution of CPR values could be observed for all the crater regions when these scatter and box plots are compared to Figures 3, 4, and supplementary figure 5 of Sinha et al.[1]

Because of the erroneous formula used, we emphasize that the CPR ranges presented in their work do not represent the true CPR values, and therefore their claim on the detection of subsurface ice from regions with elevated CPRs (>1) remains dubious.

Empirical thresholds of polarimetric radar parameters

The radar CPR provides important information on the physical characteristics of the target surface and is strongly modulated by roughness-induced changes in scattering on or beneath the surface, the viewing geometry, and the dielectric properties of the target (**ref. 3, 4)**. The degree of polarization can be effectively used to characterize the nature of the targets that backscatter the radar waves (e.g. **ref. 5**). The radar wave is totally depolarized for DOP=0, totally polarized for DOP=1, and for partially polarized waves, 0<DOP<1. When considering radar backscatter from sheet-like clean water ice, at least a few radar wavelengths thick, the material's low microwave loss can lead to strong radar backscatter and

enhanced CPR due to forward scattering by embedded dielectric contrasts (e.g., cracks and voids). Such enhanced radar signatures, observed from the poles of Mercury (**ref. 6**) and icy Galilean satellites (**ref. 7**) can be modelled as a coherent backscatter effect (CBE, **ref. 8).** For CBE to occur, the radar waves have to travel a given scattering path but in opposite directions, and emerge with the same phase shift along both directions and constructively interfere, which boosts the intensity in both radar backscatter and the CPR (**ref. 7**). It is important to note here that while, in general, multiple scattering acts to depolarize an incident radar signal (e.g. due to wavelength-scale roughness), the coherent enhancement near the backscatter direction will be stronger in the incident polarization sense since the individual scattering events, especially for forward scatterers, will preserve the polarization (**ref. 8**). This implies that CBE associated with slab-like water ice deposits will exhibit enhanced CPR (>1) combined with DOP values approaching unity. In effect, the correlation of low DOP (< 0.13) combined with high CPR values (>1) as the criterion set by Sinha et al[1] becomes invalid, for detecting thick, clean water ice signatures from the south polar lunar craters.

Furthermore, we compared the polarimetric radar properties of crater F2 (1.1 km in diameter), for which **ref.1** suggested the strongest evidence of subsurface ice within Faustini PSR, with those of two non-polar craters Tycho (fresh, Copernican age, 85 km in diameter) and Byrgius C (non-polar anomalous crater, 13 km in diameter, **ref. 9**). For this analysis, we sampled a portion of impact melt associated with Tycho crater's northern ejecta blanket and the interior of Byrgius C crater (supplementary Figure S3), and both regions have abundant cm-to-m scale rocks. For the sampled regions from these three crater regions, we generated (i) CPR vs DOP 2-D density distribution in terms of kernel density estimate (KDE) contour plots along with their histograms, (ii) ordinary least squares (OLS) and standardised major axis (SMA) fits of σ°_{SC} vs. σ°_{OC} along with their Spearman correlation coefficients (ρ_s), and (iii) Bhattacharya Coefficients (BC) to quantify the overlap between the joint distributions of variable pairs CPR-DOP and σ°_{SC} - σ°_{OC}. The comparison is shown in Figure 2 and we observe that:

1. In the CPR-DOP KDE contours (Figure 2a), all three crater regions share some overlap in their outer contours, particularly in the CPR range 0.5–1.2 and DOP range 0.1–0.4, and have comparable mean CPR (~1.01–1.12) and low DOP (~0.25–0.32) values. Despite the visible contour offset of F2 (Faustini), its CPR-DOP distribution shares ~90% overlap with the other two, reflecting that the tails of all distributions cover a broad shared region even if their cores differ. Moreover, the low 'ρ_s' values (Figure 2c-column 4) indicate a weak, almost negligible, monotonic relationship between CPR and DOP, and they vary largely independently of each other for all the crater regions. Additionally, all three pairwise BC values are high (Figure 2d)—indicating substantial distributional overlap in CPR-DOP space across all pairs, signifying that all three regions share a common scattering regime in terms of depolarization of the radar waves.
2. A comparison of σ°_{SC} and σ°_{OC} values is a better diagnostic tool than the CPR parameter, in order to understand the near-surface physical and dielectric properties of a target surface (**ref. 4**). Along with OLS, we also performed SMA regression for the σ°_{SC} vs. σ°_{OC} values in order to minimize residuals in both directions and yield an unbiased estimate of the proportional relationship between

them. The three SMA best-fit lines (Figure 2b) fan out progressively — Byrgius C closest to the 1:1 line, F2 (Faustini) intermediate, and Tycho most divergent — indicating an increasing degree of σ°_{OC} dominance over σ°_{SC} in that order. The pairwise BC values in σ°_{SC}-σ°_{OC} space (Figure 2d; 0.389–0.913) show that while Byrgius C and Faustini are nearly co-located, Tycho is substantially separated from both, driven primarily by its much higher absolute backscatter magnitude extending to σ°_{OC} and σ°_{SC} values nearly twice those of the other two crater regions.

To summarize, the three regions are more similar to each other in CPR-DOP space than in σ°_{SC}- σ°_{OC} space, with Tycho region being the primary source of σ°_{OC} -σ°_{SC} divergence. This behaviour is consistent with the known surface rock abundances for Tycho and Byrgius C regions. Tycho impact melt has abundant centimetre-to-metre scale rocks and boulders, reflecting strong depolarization and complex multiple-bounce scattering from a rough, rock-rich surface (**ref. 10**). For Byrgius C interior, these trends suggest a surface with comparatively low meter-scale but greater wavelength-scale rock abundance with similar contributions from single and multiple scattering components (**e.g. ref 9**). The crater F2 (Faustini) occupies a transitional position in both CPR-DOP and σ°_{SC}- σ°_{OC} space — consistent with a surface having intermediate roughness between the other two regions analysed here.

We conclude that i) regions of enhanced CPR from the doubly shadowed craters identified by Sinha et al.[1] can be better explained by roughness-induced changes in the radar backscatter; and ii) a robust evidence for thick, sheet-like water ice within the lunar poles require a combination of strong radar linear and circular polarization ratios, and enhanced DOP values, along with a high degree of correlation between radar-bright features and regions of permanent shadow (e.g. **ref 6, 8**).

Declarations

Data Availability

Raw and calibrated Chandrayaan-2 Dual-Frequency Synthetic Aperture Radar (DFSAR) data is available publicly at the Chandrayaan-2 portal of the ISRO Science Data Archive (ISDA) at https:/pradan.issdc.gov.in/ch2

Code Availability

No new code to analyse, process DFSAR data is developed for this work. Python codes used for generating plots shown in figure 2 can be provided by the corresponding author upon request

Competing Interests

The authors of this work declare that they have no competing interests.

Author contributions

S.B. led the conceptualization of the study and contributed to data analysis, original draft, and scientific interpretation. T.C. and R.M. curated the data, generated the circular polarization ratio (CPR) and degree of polarization (DOP) images and contributed to data analysis. B.J.T. and E.G.R-V contributed to original draft, scientific discussions, and statistical interpretations. D.P provided overall guidance and resources. All authors have read and approved the manuscript.

Acknowledgements

We would like to thank the instrument and data processing teams of Chandrayaan-2 DFSAR at Space Applications Centre, ISRO, for their efforts in realizing the instrument and generating user-ready processed datasets.

References

1. Sinha RK, Bharti RR, Acharyya K, Mishra SK, Srivastava N, Bhardwaj A (2026) Subsurface ice in doubly shadowed craters as revealed by Chandrayaan-2 dual frequency synthetic aperture radar. npj space Explor 2:22, 1–27. https://doi.org/10.1038/s44453-026-00038-9
2. Campbell BA (2002) Radar Remote Sensing of Planetary Surfaces. Cambridge University Press, Cambridge, U.K
3. Campbell BA (2012) High circular polarization ratios in radar scattering from geologic targets. J Geophys Res 117:E06008. https://doi.org/10.1029/2012JE004061
4. Virkki A, Bhiravarasu SS (2019) Modeling radar albedos of laboratory-characterized particles: Application to the lunar surface. J Geophys Res 124:3025–3040. https://doi.org/10.1029/2019JE006006
5. Raney RK, Cahill JTS, Patterson GW, Bussey DB (2012) J. The *m-chi* decomposition of hybrid dual-polarimetric radar data with application to lunar craters. J Geophys Res 117. https://doi.org/10.1029/2011JE003986
6. Harmon JK et al (1994) Radar mapping of Mercury's polar anomalies. Nature 369:213–215. https://doi.org/10.1038/369213a0
7. Black GJ, Campbell DB, Nicholson PD (2001) Icy Galilean satellites: Modeling radar reflectivities as a coherent backscatter effect. Icarus 151:167–180. https://doi.org/10.1006/icar.2001.6616
8. Peters K (1992) The coherent backscatter effect: A vector formulation accounting for polarization and absorption effects and small or large scatterers. Phys Rev B 46:801–812
9. Fa W, Cai Y (2013) Circular polarization ratio characteristics of impact craters from Mini-RF observations and implications for ice detection at the polar regions of the Moon. J Geophys Res 118:1–27. https://doi.org/10.1002/jgre.20110
10. Carter LM, Neish CD, Bussey DBJ, Spudis PD, Patterson GW, Cahill JTS, Raney RK (2012) Initial observations of lunar impact melts and ejecta flows with the Mini-RF radar. J Geophys Res 117:E00H09. https://doi.org/10.1029/20011JE003911

11. Neumann GA (2011) LRO Moon Laser Altimeter 4 GDR V1.0, Dataset https://doi.org/10.17189/1520642
12. Bhiravarasu SS et al (2021) Chandrayaan-2 dual-frequency synthetic aperture radar (DFSAR): Performance characterization and initial results. Planet Sci J 2(4):134–154. https://doi.org/10.3847/PSJ/abfdbf
13. Zebker HA, Lou Y (1990) Phase calibration of imaging radar polarimeter Stokes matrices. IEEE Trans Geosci Remote Sens 28(2):246–252. https://doi.org/10.1109/36. 46704
14. Lee J-S, Pottier E (2009) Polarimetric Radar Imaging: From Basics to Applications. CRC, Boca Raton, FL
15. Raney RK (2006) Dual-polarized SAR and stokes parameters. IEEE Geosci Remote Sens Lett 3:317–319. https://doi.org/10.1109/LGRS.2006.871746

Figures

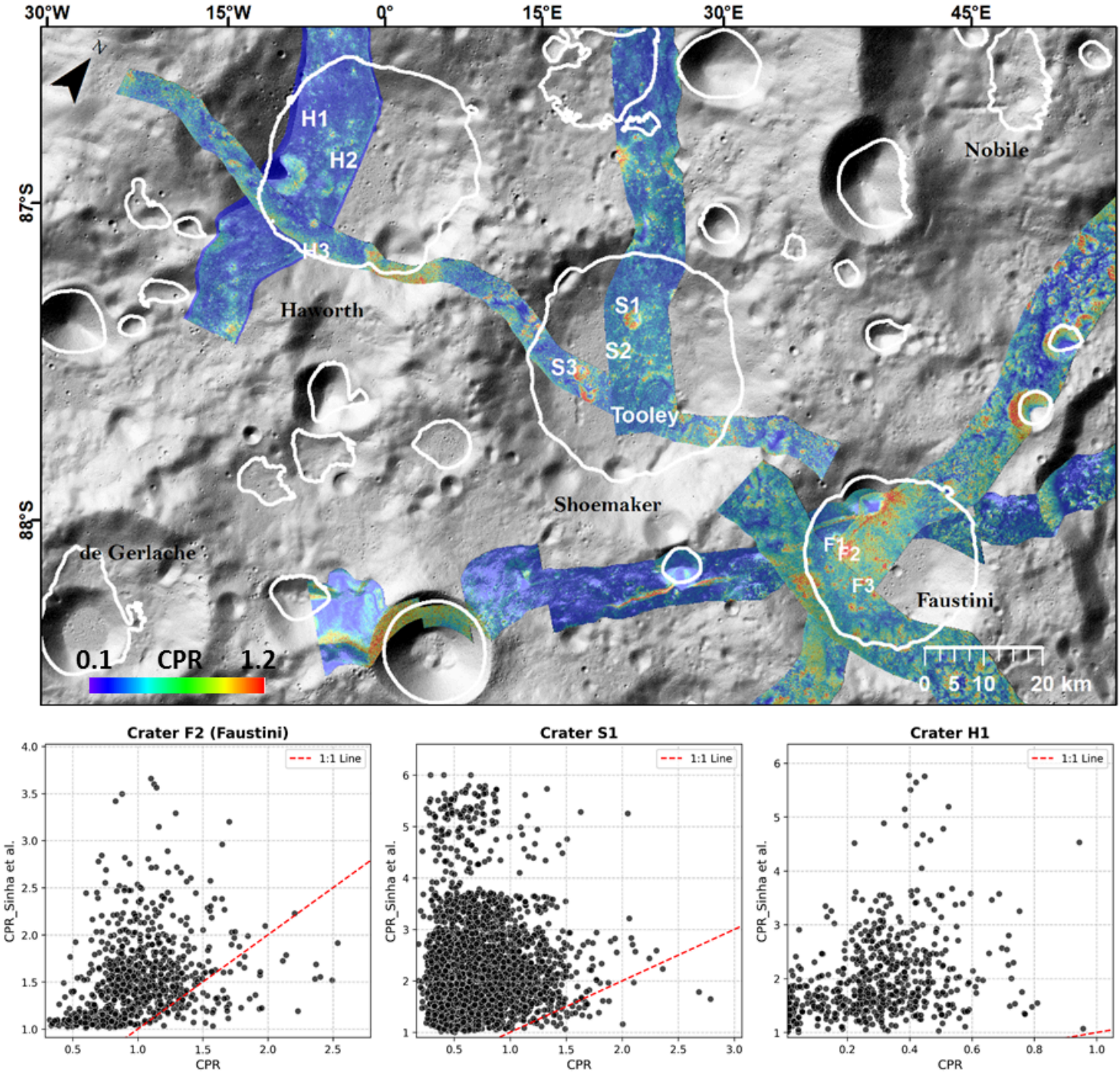
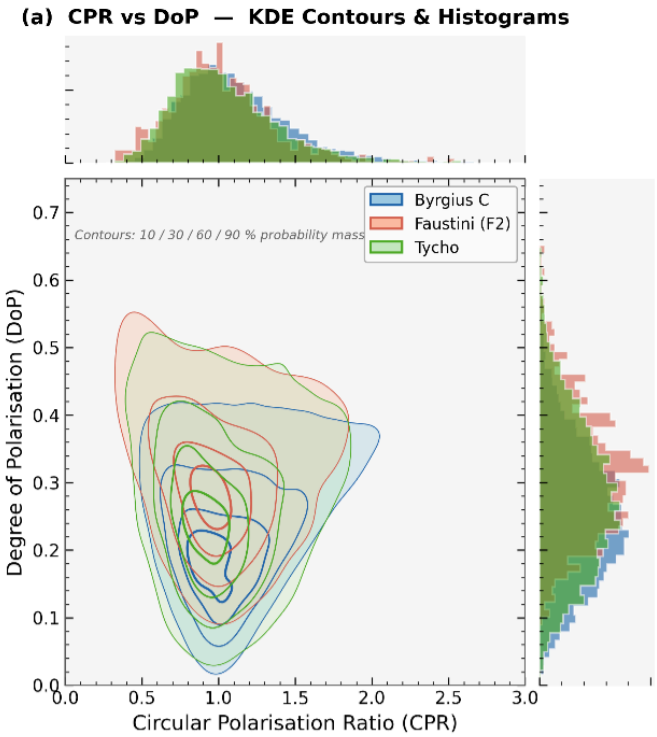
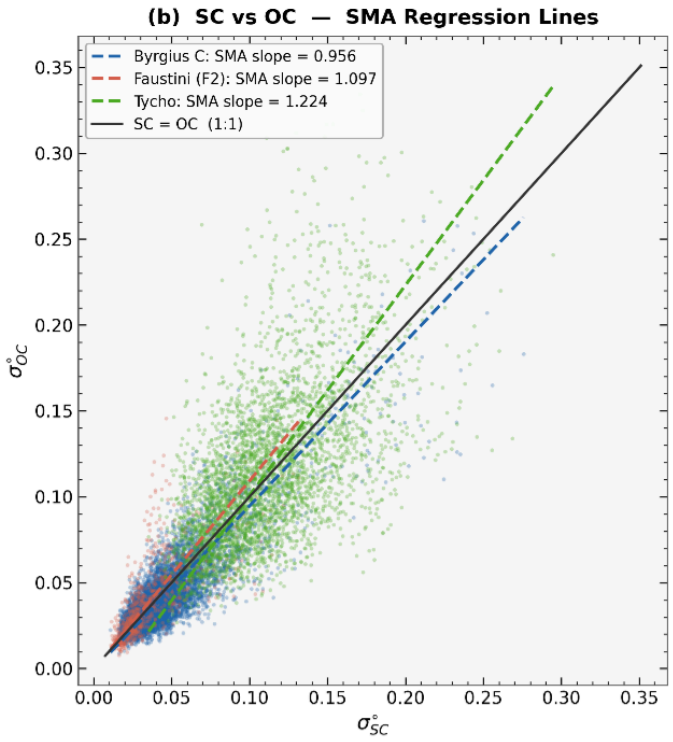


Figure 1

Top: DFSAR circular polarization ratio (CPR) images covering the doubly shadowed craters analysed by Sinha et al[1]. The CPR images are stretched to a colour scale [shown at the bottom left, from violet (0.1) to red (1.2 and above)] and are overlain on a LOLA DEM-based hillshade image of the South Polar Region. Crater names are indicated and the white polygons represent the permanently shadowed regions (PSRs). Bottom: Scatter plots of CPR (correct method, x-axis) vs. CPR (Sinha et al[1], y-axis.) for interior of three craters F2 (Faustini), S1, and H1. The red dashed line in each plot represent the x=y trend.





(c) Crater-wise Statistics (with Spearman ρ_s)

Site	CPR (mean±σ)	DoP (mean±σ)	CPR-DoP ρs	SC-OC OLS slope	SC-OC SMA slope	SC-OC ρs
Byrgius C	1.12±0.4	0.25±0.1	0.185	0.808	0.956	0.764
Faustini (F2)	1.01±0.3	0.32±0.1	-0.165	0.812	1.097	0.831
Tycho	1.04±0.3	0.28±0.1	-0.056	0.699	1.224	0.585

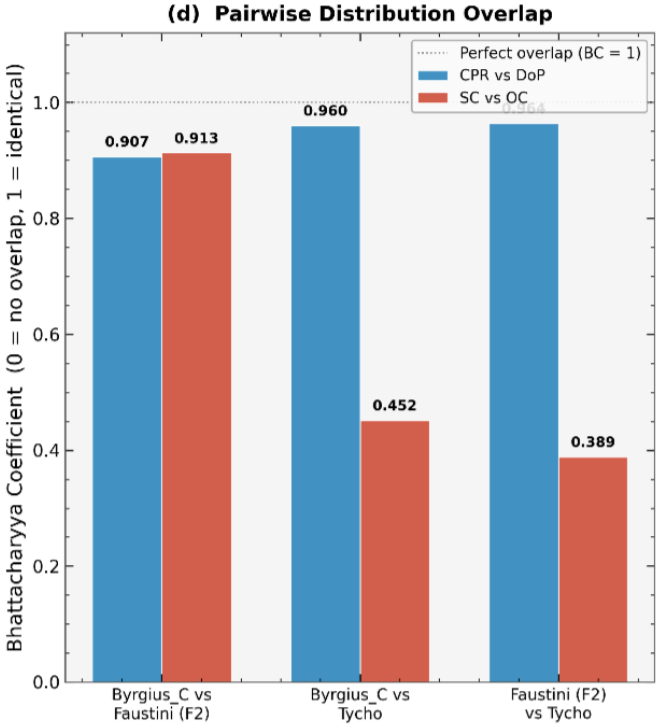


Figure 2

Statistical comparison of CPR, DOP, same-sense circular (σ°_{SC}), opposite-sense circular (σ°_{OC}) backscatter coefficients, generated from DFSAR data of Byrgius C, Faustini (F2), and Tycho crater regions. (a) Two-dimensional kernel density estimate (KDE) contours of the joint CPR-DOP distribution for each region, with contour levels enclosing 10%, 30%, 60%, and 90% of the total probability mass. Overlaid marginal histograms for both CPR (top) and DOP (right) illustrate the individual data

distributions for each region, revealing their central tendencies and spread. The different colours correspond to each crater region as defined in the legend. (b) Scatter plot of for all three regions, overlaid with Standardised Major Axis (SMA) regression lines (dashed) and the 1:1 reference line (solid black). (c) Region-wise summary statistics including mean and standard deviation of CPR and DOP, Spearman correlation coefficient (ρ_s) and OLS slope for CPR-DOP, and OLS slope, SMA slope, and ρ_s for σ°_{SC}-σ°_{OC} plot. (d) Pairwise Bhattacharyya coefficients (BC) quantifying the overlap between the joint distributions of each region pair in CPR-DOP and σ°_{SC}- σ°_{OC} space, where BC = 1 indicates identical distributions and BC = 0 indicates no overlap.

Supplementary Files

This is a list of supplementary files associated with this preprint. Click to download.

- Supplementaryinfonpjv4.pdf